ACS SENSORS

Article

Cite This: ACS Sens. 2017, 2, 1796−1804

pubs.acs.org/acssensors

Subradiant Dipolar Interactions in Plasmonic Nanoring Resonator Array for Integrated Label-Free Biosensing

Yuzhang Liang,[†] Hui Zhang,[†] Wenqi Zhu,[‡,§] Amit Agrawal,[‡,§] Henri Lezec,[‡] Lixia Li,[∥] Wei Peng,[∥] Yi Zou,[†] Yanqing Lu,*[,†] and Ting Xu*[,†]

[†]National Laboratory of Solid State Microstructures, College of Engineering and Applied Sciences, Collaborative Innovation Center of Advanced Microstructures, Nanjing University, Nanjing 210093, China

[‡]Center for Nanoscale Science and Technology, National Institute of Standards and Technology, Gaithersburg, Maryland 20899, United States

[§]Maryland NanoCenter, University of Maryland, College Park, Maryland 20742, United States

[∥]College of Physics and Optoelectronics Engineering, Dalian University of Technology, Dalian 116024, China

Supporting Information

ABSTRACT: With the development of advanced nanofabrication technologies over the past decade, plasmonic nanostructures have attracted wide attention for their potential in label-free biosensing applications. However, the sensing performance of nanostructured plasmonic sensors is primarily limited by the broad-line-width features with low peak-to-dip signal ratio in the extinction spectra that result from strong radiative damping. Here, we propose and systematically investigate the in-plane and out-of-plane dipolar interactions in an array of plasmonic nanoring resonators that are from the spatial combination of classic nanohole and nanodisk structures. Originating from the strong coupling of the dipolar modes from parent nanohole and nanodisk structures, the subradiant lattice plasmon resonance in the nanoring resonator array exhibits narrow-line width spectral features with high peak-to-dip signal ratio and strong near-field electromagnetic enhancement, making it an ideal platform for high-sensitivity chemical and biomedical sensing. We experimentally demonstrate that the plasmonic nanoring resonator array can be used for high-sensitivity refractive index sensing and real-time monitoring of biomolecular specific binding interactions at nanomolar concentration. Moreover, due to its simple normal incident illumination scheme and polarization independent optical response, we further transfer the plasmonic nanoring resonator array onto the optical fiber tip to demonstrate an integrated and miniaturized platform for label-free remote biosensing, which implies that the plasmonic nanoring resonator array may be a potential candidate for developing high performance and highly integrated photonic biosensing systems.

KEYWORDS: *plasmonic nanostructure, biosensing, dipolar interaction, fiber optics, protein binding, point of care diagnostics*

Localized surface plasmon resonance (LSPR) in a variety of plasmonic nanostructures, such as discrete metallic nanodisks and nanoparticles, have received significant attention for their potential in low-cost, label-free biosensors.[1−21] In contrast to the conventional propagating surface plasmon based sensors relying on bulky prism-coupling mechanism,[22−24] the size of nanostructured LSPR sensors can be reduced to the micrometer scale. This makes them very attractive for the design of portable devices for point-of-care testing (POCT) application.[25] In contrast to the centralization and increased efficiency in laboratory diagnostics, POCT shortens the time of transport and preparation of clinical samples and biochemical-test results are rapidly available at the point of care. But unfortunately, the sensing performance of LSPR sensor is always limited by the broad-line width features with low peak-to-dip signal ratio in the extinction spectra resulting from strong radiative damping, which significantly limits the intensity of localized electromagnetic fields around the isolated nanostructures.[26,27] Hence, the quest to suppress the radiative damping is essential in the research field of plasmonic biosensing. Recent works have suggested that by carefully engineering plasmonic nanostructures, such as concentric nanocavity[28−30] and closely packed nanoparticle cluster,[31−34] higher localized electromagnetic fields and narrower line-shape can be achieved for subradiant plasmon resonance, which in principle can be used to improve the sensing performance.

Another effective approach to manipulate plasmon line width spectral features of nanostructures is to assemble them into an array. Because optical energy scattered by one nanostructure unit cell will be captured by neighboring nanostructure as plasmon instead of decaying as free-space propagating light, the array exhibits completely different optical responses from those of an isolated nanostructure. Recently, it has been demonstrated that strongly coupled one- and two-dimensional nanostructure arrays can produce narrow lattice plasmon resonance by suppressing radiative losses.[35−38] Therefore,

Received: August 23, 2017
Accepted: November 15, 2017
Published: November 15, 2017

DOI: 10.1021/acssensors.7b00607
ACS Sens. 2017, 2, 1796−1804

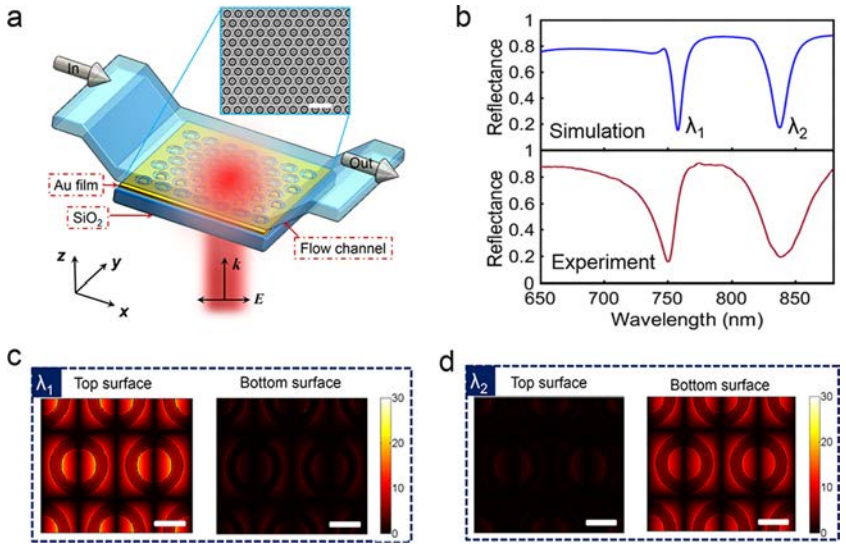

Figure 1. Geometry and optical characteristics of Au PNRA. (a) Schematic representation of the miniaturized PNRA sensor device with a fluid flow channel and a top-down scanning electron microscopy image of the fabricated PNRA (Scale bar, 2 μm). The periodicity (P) of the PNRA is 640 nm and the thickness of the Au film is 100 nm. The inner radius (r) and outer radius (R) of the nanoring are 150 and 240 nm, respectively. (b) The theoretical (blue solid line: FDTD simulation) and experimental (red solid line) reflectance spectra. Electric field $|E|$ distribution on the top and bottom surfaces of nanoring array at resonant wavelengths (c) λ_1 and (d) λ_2. Scale bar, 300 nm.

nanostructure arrays supporting subradiant lattice plasmon resonance have emerged as a powerful photonic platform for sensing applications.

Here, we develop a novel, high-sensitivity label-free biosensing platform based on a plasmonic nanoring resonator array (PNRA), which is constructed from the spatial combination of nanohole and nanodisk arrays. Based on coupled dipole theory, the in-plane and out-of-plane strong coupling of the dipolar modes from parent nanohole and nanodisk structures in PNRA generates a sharp subradiant lattice plasmon resonance with an extremely narrow line width (~7 nm), a high peak-to-dip signal ratio (0.7), and high refractive index sensitivity (~545 nm RIU^{-1}). The PNRA device are utilized here to experimentally achieve high sensitivity microfluidic refractive index sensing and real-time monitoring of biomolecular interaction between Ribonuclease B (RNase B) and Concanavalin A (Con A) protein molecules at ultralow concentrations. Importantly, compared to previous works that use complicated angular illuminations and specific polarizations to excite high-order guide modes in metamaterials[39,40] or optical Fano resonances in nanostructures for sensing,[41−43] the subradiant fundamental lattice plasmon resonance in PNRA can be excited by using normally incident randomly polarized light and generates a stable spectral lineshape with a high peak-to-dip signal ratio around the resonant wavelength. This implies that our device is able to be conveniently probed where the incident and reflected light are efficiently collected by the same optical path. As a proof-of-concept demonstration, we successfully transfer the PNRA onto the tip of an optical fiber for further miniaturization and integration. The sensing performance of optical fiber sensor with PNRA confirms it as a robust tool for remotely detecting biomolecules interaction.[44−47]

RESULTS

Fabrication and Characterization of PNRA. The schematic diagram of the designed PNRA biosensor is depicted in Figure 1a. The structure can be regarded as the spatial combination of simple nanohole and nanodisk arrays arranged in a hexagonal lattice, where the gap between nanohole and nanodisk forms a nanoring. Due to the axial symmetry of the structure, the optical properties of PNRA are independent of the polarization direction of the normally incident light. The reflectance spectrum of the structure is investigated using full-wave simulation based on the finite-difference time-domain (FDTD) algorithm. The structural parameters are as follows: periodicity P = 640 nm, inner radius r = 150 nm, outer radius D = 240 nm, and the thickness of Au film is 100 nm. The top surface of the PNRA is covered with a medium having a refractive index (RI) of 1.331 to match that of the aqueous solution in experiment. The calculated reflectance spectrum is plotted in Figure 1b (blue solid line), where the two resonance dips can be observed at wavelengths of λ_1 = 758 nm and λ_2 = 838 nm. The reflectance dip at λ_1 has a full-width at half-maximum (fwhm) line width of ~7 nm, which results in a quality factor (Q-factor) that reaches ~108. The reflectance dip at λ_2 has ~14 nm fwhm and ~60 Q-factor (see Methods for details on the extraction of fwhm and Q-factor).

Inset of Figure 1a shows the top-down scanning electron microscopy (SEM) image of the fabricated sample. Before the optical measurements, the top surface of the PNRA is immersed in an aqueous solution with a polydimethylsiloxane (PDMS) flow cell. The fabricated structure is illuminated with a randomly polarized normally incident white light from the substrate side. The experimentally measured reflectance spectrum is depicted in Figure 1b (red solid line), where two resonance dips are also observed at the wavelengths of 750 and 838 nm. The measured fwhm and Q-factor of the resonance dip at λ_1 (λ_2) are ~15 nm (~40 nm) and ~50 (~21), respectively. The relative wider fwhm and lower Q-factors achieved in experiment can be attributed to three factors: First, surface roughness of fabricated structure is limited by the grain sizes of multicrystalline gold film produced by vacuum coating, which introduces scattering losses. Second, the geometry parameters of the fabricated sample in experiment are slightly different from those of simulated model. For example, outer radius (D)

DOI: 10.1021/acssensors.7b00607
ACS Sens. 2017, 2, 1796−1804

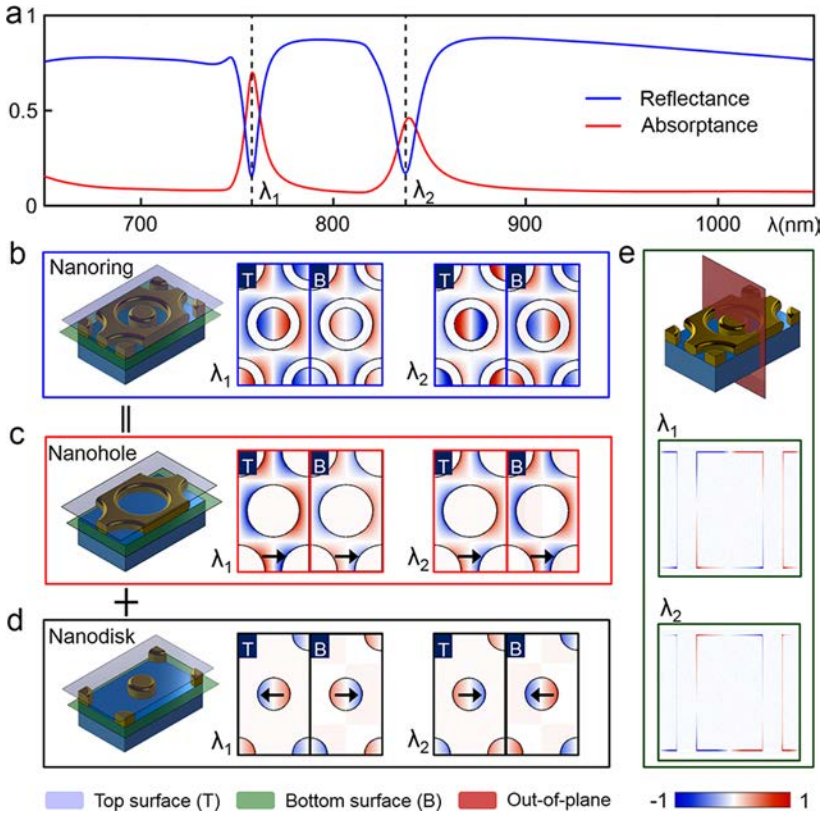

Figure 2. Dipolar interactions in the PNRA. (a) Calculated reflectance (absorptance) spectrum of the PNRA with periodicity P = 640 nm, inner radius r = 150 nm, outer radius D = 240 nm, and Au film thickness 100 nm. The calculated in-plane normalized surface charge distributions of the relevant modes at both top and bottom surfaces of (b) nanoring, (c) nanhole, and (d) nanodisk arrays at resonant wavelengths λ_1 and λ_2, where the directions of dipolar modes are indicated by the black arrows. (e) Calculated out-of-plane normalized surface charge distributions of PNRA at resonant wavelengths λ_1 and λ_2. The top and bottom surfaces and out-of-plane are indicated by blue, green, and red planes, respectively. To clearly exhibit out-of-plane normalized surface charge distributions, Figure 2e is plotted out-of-scale compared to the actual structure size.

of nanoring array in experiment may be larger than that of numerical simulation. As shown in Figure S1a, we theoretically find that the line-shape of resonant wavelength λ_1 becomes wider with the increase of outer radius. Third, an objective lens with a numerical aperture (NA) of 0.10 is used for the spectral measurements. A nonzero NA objective results in sample excitation at oblique incidence angles, which decreases the spatial coherence among different modes and generates a wide spectral line-shape in experiment.[48,49] The simulated and measured reflectance spectra for a different outer radius of the nanoring and using a different numerical aperture of the objective are shown in Figure S1b. Nevertheless, both the spectral line-shape and the position of the resonance dips measured in the experiment are in good agreement with those calculated using FDTD simulation. Figure 1c,d depicts electric field distribution on the top and bottom surfaces of nanoring array at resonant wavelengths λ_1 and λ_2, respectively. For resonance wavelength λ_1, the electric field is mainly localized on the top surface of the PNRA structure. However, the electric field is mainly localized at the bottom surface for resonance wavelength λ_2. This indicates that two dips of the reflectance spectrum not only show frequency separation, but the spatial localization of optical energy is also separated. These characteristics make the PNRA structure very useful for the design of plasmonic sensors.

Theoretical Analysis of Dipolar Interactions in PNRA. The calculated reflectance (absorptance) spectrum of the PNRA exhibits two resonance dips (peaks) at λ_1 = 758 nm and λ_2 = 838 nm, as shown in Figure 2a. These two resonance dips can be qualitatively explained by using plasmonic hybridization theory.[50−53] To further understand these resonances in detail, we first calculate the in-plane normalized surface charge distributions of the relevant modes at both top and bottom surfaces of nanoring, nanhole, and nanodisk arrays at resonant wavelengths λ_1 and λ_2 (Figure 2b−d). As expected, the mode distributions of PNRA are exactly the spatial superposition of the in-plane dipolar modes, respectively, from nanohole and nanodisk structures. At resonant wavelength λ_1, dipolar modes at the top surfaces of nanohole and nanodisk structures have opposite orientations. The antiparallel dipolar interaction reduces the total dipole momentum and minimizes the radiative damping of the PNRA system, which is a typical subradiant characterization.[28,29] As a result, antiparallel dipolar at the top surface can effectively trap the incident light and excite subradiant lattice plasmon resonance, resulting in a large narrow-line-width absorbance peak at λ_1. On the other side, in-plane dipolar modes at the bottom surfaces of nanohole and nanodisk structures are oriented in the same direction at λ_1. The parallel dipolar interaction enhances the total dipole momentum and results in a rapid depletion of the plasmon energy. Compared with the top surface, the optical intensity at the bottom surface of a PNRA is much weaker (Figure 1c). Therefore, the enhanced optical field at the top surface for resonance wavelength λ_1 is sensitive to the change of ambient environment, which can be used for a sensing application.

DOI: 10.1021/acssensors.7b00607
ACS Sens. 2017, 2, 1796−1804

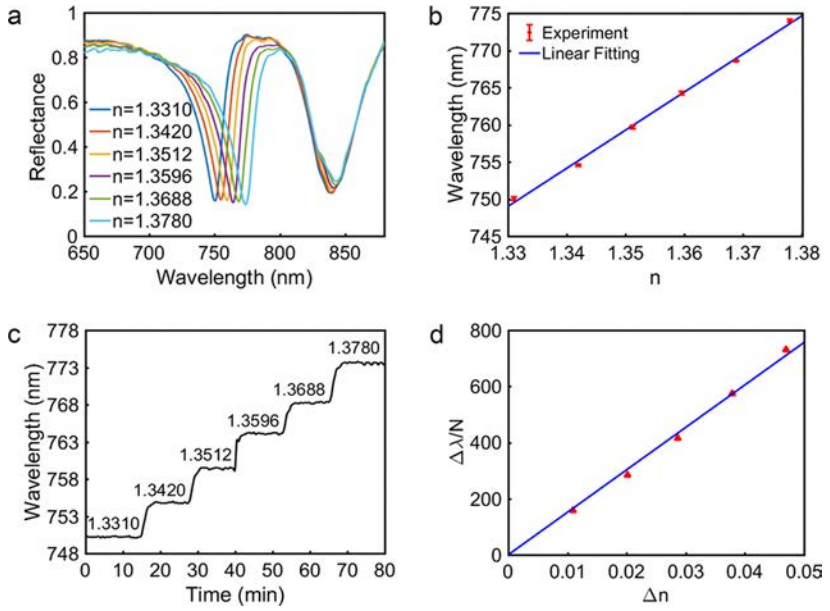

Figure 3. Evaluation of PNRA sensor device integrated with microfluidics. (a) Measured reflectance spectra of the sensor device for different refractive index of sodium chloride solutions. (b) Relationship between experimentally measured resonance dip position and the refractive index. Uncertainties in (b) are based on the standard deviations of five repeated measurements for every experimental data point. The upper and lower limits of the error bar in (b) are too small to be clearly seen. (c) Wavelength shifts of dip for different refractive index of sodium chloride solutions as a function of time. (d) The relationship between wavelength shifts normalized experiment noise (N) and refractive index change in order to evaluate the limit of detection for a PNRA.

Contrary to λ_1, the dipolar interactions at resonant wavelength λ_2 are opposite: parallel dipolar interactions occur at the top surface while antiparallel dipolar interactions occur at the bottom surface. Therefore, the optical energy is mainly localized at the bottom surface of PNRA at the wavelength of 838 nm (Figure 1d). Because the bottom surface of PNRA is glass substrate and not in contact with the microfluidics, the plasmon resonance at λ_2 cannot be used for sensing applications. Moreover, the optical field at the top surface for resonance wavelength λ_2 is immune to the ambient environment, which can serve as a self-reference channel for sensing detection.

Besides investigating the in-plane dipolar interactions, we also calculate the out-of-plane normalized surface charge distributions of PNRA at resonant wavelengths λ_1 and λ_2, as shown in Figure 2e. It can be clearly seen that at the resonant wavelengths, the normalized surface charge distributions, respectively, form an out-of-plane dipolar (quadrupolar) mode for the parent nanohole (nanodisk) structure. The out-of-plane quadrupolar mode in nanodisk array originates from the geometry-dependent dipolar interaction between large nanoparticle structures arranged in a two-dimensional array.[38] Due to the interference between out-of-plane dipolar and quadrupolar modes, the PNRA exhibits a Fano-like asymmetric peak-and-dip spectral profile at resonance and strongly localizes the optical field around the structure. As shown in Figure S2, the absorption and optical field intensity at the top surface of the PNRA are much stronger than those of pure nanohole and nanodisk structures at the resonant wavelengths, which is beneficial for sensing applications. This optical field primarily overlaps with the volume containing the material to be sensed, satisfying an important criterion for development of a plasmonic sensor with high figure-of-merit (FOM).

Sensing Performance of the PNRA. To examine the real-time sensing performance of the PNRA as a refractive index sensor, a microchannel-based miniaturized biosensor platform is fabricated by assembling a microfluidic system on top of the PNRA. To calibrate and determine the detection limit of the sensor, sodium chloride (NaCl) solutions with refractive indices (RIs) of 1.3310, 1.3420, 1.3512, 1.3596, 1.3688, and 1.3780 are manually injected into the flow channel using a peristaltic pump at a constant flow rate of 0.2 mL/min. The RIs of the sodium chloride solutions are calibrated using an Abbe refractometer. The measured reflectance spectra of the PNRA coated with NaCl solutions of different RIs are shown in Figure 3a. As the RI of the injected solution increases, a red shift of the resonance dip around the wavelength of 750 nm occurs. For the second resonance dip around the wavelength of 838 nm, because the optical intensity localized at the bottom surface is noncontact with NaCl solutions, no variation in the measured spectrum is observed. Within the investigated RI range, the line-shape of the fundamental lattice plasmon resonance does not vary and keeps a very high peak-to-dip signal ratio, indicating a stable operation of the sensing device. The FDTD calculated reflectance spectra for an equivalent change in the bulk refractive index of the media surrounding that PNRA are shown in Figure S3a. The calculated spectral resonance line-shape and its location exhibit good agreement with the experimental results. The peak-to-dip signal contrast around the resonant wavelength, SC, defined as SC = $R_{peak} - R_{dip}$, is an important parameter associated with the signal-to-noise ratio of the sensing devices. Compared to that of nanohole and nanodisk structures (Figure S4), the SC of the PNRA structure (~0.7) is higher in simulation and experiment thanks to the highly localized optical fields caused by the subradiant dipolar interactions. This value is several times higher than that of other nanostructured plasmonic sensors[9,10,29,31,35,38] and will be beneficial for easily detecting and distinguishing the sensing signal from background noise.

DOI: 10.1021/acssensors.7b00607
ACS Sens. 2017, 2, 1796−1804

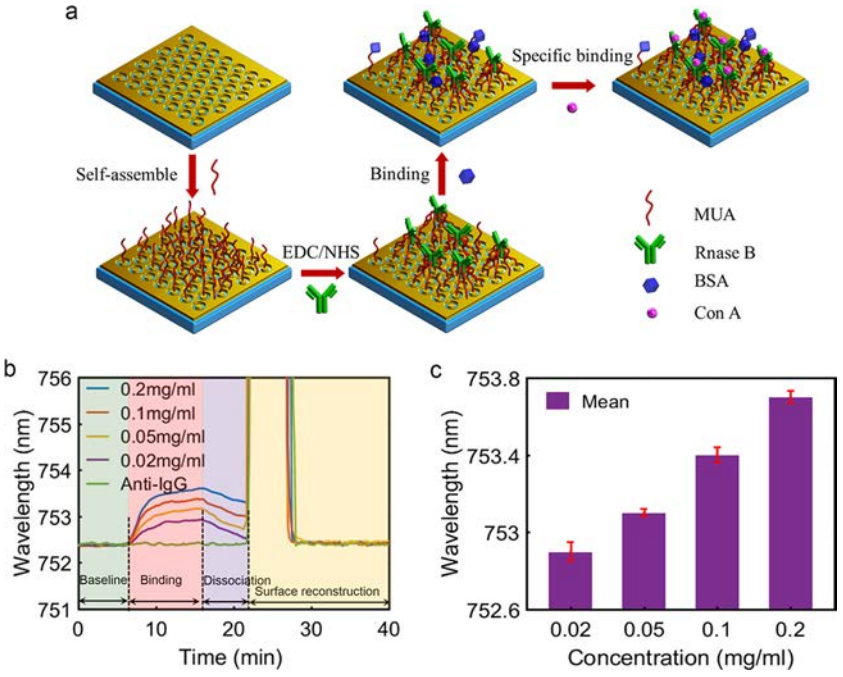

Figure 4. PNRA as a label-free biosensor to detect protein biomolecule. (a) Experiment detection flow-chart for the specific binding of Con A and Rnase B. (b) Real-time biomolecular interaction response for the detection of Con A at the concentrations of 0.02, 0.05, 0.1, and 0.2 mg/mL. The turquoise line shows the nonspecific binding of Rnase B and anti-IgG of 0.1 mg/mL. (c) Relationship between the measured wavelength positions and Con A concentration. Each measurement at a given concentration is repeated three times. The mean and standard deviation are calculated.

Besides peak-to-dip signal ratio, we also analyze another three critical parameters: RI sensitivity, figure of merit (FOM), and limit of detection (LOD) to quantitatively evaluate the sensing performance of the device. RI sensitivity, S, is defined as the resonance wavelength shift, $\Delta\lambda$, for a change in the bulk RI, Δn (i.e., $S = \Delta\lambda/\Delta n$). The spectral-dip location in the reflectance spectra as a function of RI is plotted in Figure 3b. A RI sensitivity of 513 nm RIU^{-1} is obtained by calculating the slope of the linear-fit to the experimental results, which agrees well with the calculated sensitivity of 545 nm RIU^{-1} as shown in Figure S3b. Furthermore, we respectively calculate the influence of structure parameters of nanoring array (including periodicity P, inner radius r, and outer radius R) on resonant wavelength λ_1 and RI sensitivity. The results have been plotted in Figure S5. These results indicate both resonant wavelength λ_1 and RI sensitivity increase linearly with increased periodicity. In order to achieve the sensing detection of PNRA structure at the visible frequency, the periodicity $P = 640$ nm is selected in the paper. With fixed structure periodicity, optimized RI sensitivity can be obtained by appropriate selection of the size of inner and outer radii. In addition, the change of inner and outer radii could also significantly influence the peak-to-dip signal ratio at the resonant wavelength λ_1. FOM, defined as FOM = $S/(2\gamma)$ (the sign 2γ refers to the fwhm of the resonance dip obtained in the Q-factor extraction), is a widely accepted metric that determines the sensitivity performance of an optical sensor, and is inversely proportional to the spectral sharpness of resonance. Experimentally measured FOM value is ~35 RIU^{-1} (Figure S6), which is several times higher than the FOM achieved with nanoparticle-based plasmonic sensors.[4−7,32,43] The FDTD calculated FOM value of ~78 RIU^{-1} is a factor of 2 higher than the experimentally measured values due to a wider $\Delta\lambda$ obtained in experiment. In principle, the experimental FOM can be further improved by optimizing nanofabrication techniques to achieve smaller metal scattering losses, or by using a lower NA objective lens in the measurement.

In addition to the RI sensitivity and FOM, LOD is also a key parameter for characterizing the performance of a sensing device. The LOD is defined as LOD = $N/S = \Delta n/(\Delta\lambda/N)$, where S is RI sensitivity and N refers to the experimental spectral noise. In our experiment, N is obtained by calculating the standard deviation of the experimental signal for a duration of 80 min with a time resolution of 5 s. Figure 3c shows the real-time response of the resonance dip for NaCl solution with different RI. Using the measured data shown in Figure 3c, the experiment noise N for different RI solutions is 0.0674, 0.0608, 0.0718, 0.0714, 0.0628, and 0.0656 nm, respectively. Therefore, based on the relationship between the signal-to-noise ratio $(\Delta\lambda/N)$ and the change of RI shown in Figure 3d, we can achieve a LOD of ~1.3219×10^{-4} RIU for our sensor device. This LOD value is comparable to that of the previously reported SPR sensor based on prism-coupling configuration.[54]

Real-Time Detection of Specific Binding between Protein Molecules. To further demonstrate the ability of PNRA as high-performance biosensor, we perform the experiments to detect in real-time the specific binding of RNase B and Con A protein molecules in solution on the sensing surface. The specific binding of RNase B and Con A has been extensively studied as a standard affinity model for biosensors.[55,56] To capture the Con A biomolecule at different concentrations, the fabricated PNRA sensor is functionalized with immobilized RNase B. The immobilization process of RNase B is depicted in Figure 4a. First, the sensing chip is cleaned with ultrapure water and ethanol. After a subsequent wash, the sensing substrate is dipped into an ethanol solution of 11-mercaptoundecanoic acid (MUA, 10 mM) at room temperature for 24 h to self-assemble an alkanethiol monolayer on the surface of gold layer. The unreacted thiol molecules are washed away by using ethanol. After drying under N_2 gas, a

DOI: 10.1021/acssensors.7b00607
ACS Sens. 2017, 2, 1796−1804

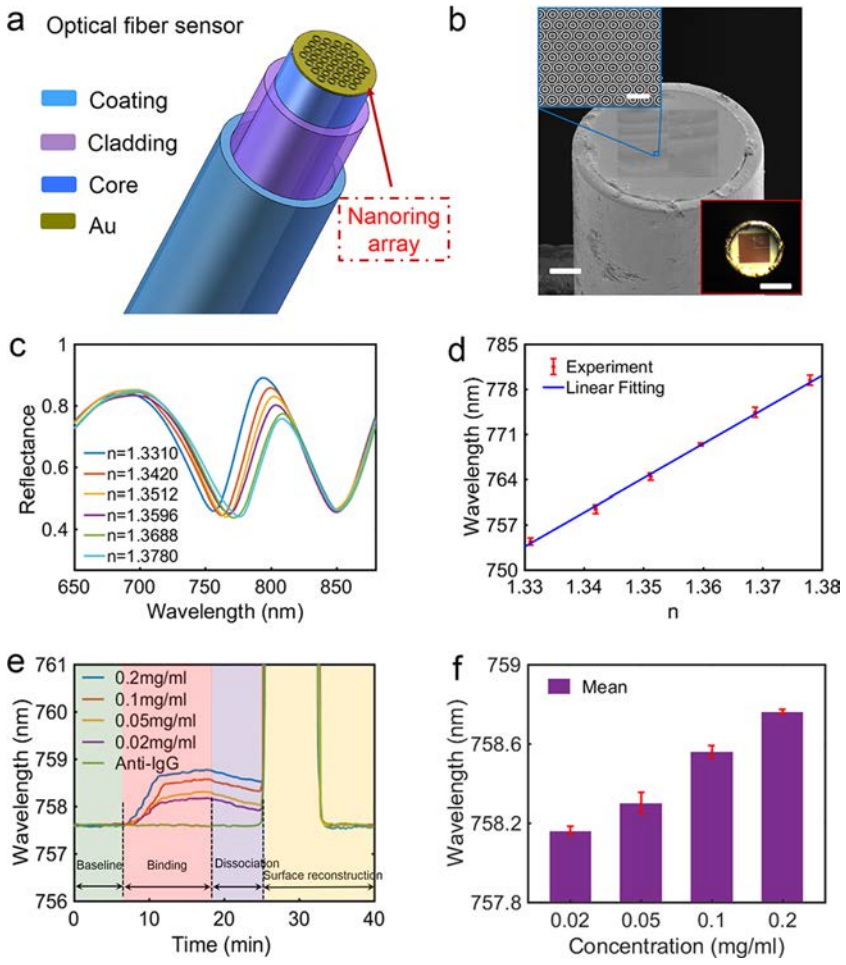

Figure 5. PNRA integrated with the optical fiber for remote biosensing. (a) Schematic representation of the optical fiber sensor device with PNRA integrated on the end face of optical fiber. (b) Oblique-view SEM images of the fabricated PNRA on the optical fiber end face. Scale bar, 50 μm. Inset at left corner is magnified SEM image. Scale bar, 1 μm. Inset at right corner is microscope image. Scale bar, 150 μm. (c) Experimentally measured reflectance spectra of the optical fiber sensor device for various refractive index of NaCl solutions. (d) Relationship between measured resonance dip position and the refractive index. Uncertainties are based on the standard deviations of five repeated measurements for every experimental data point. (e) Real-time specific detection of optical fiber sensor device for different concentrations of Con A. The turquoise line shows the nonspecific binding of RNase B and anti-IgG of 0.1 mg/mL. (f) Relationship between the measured wavelength position and Con A concentration. Each measurement at a given concentration is repeated three times.

mixed aqueous solution containing 1-ethyl-3-(3-dimethylamino-propyl) carbodiimide hydrochloride (EDC, 0.55 M) and *N*-hydroxysuccinimide (NHS, 0.5 M) is used for 30 min at 4 °C to activate the alkanethiol monolayer on the gold surface. Then, the sensing chip is rinsed with deionized water and dried under N_2 gas. After activating, the sensing chip is equipped with the microfluidic channel. The growth process of biomolecules on the surface of the structure is dynamically monitored in real time. 0.1 mg/mL RNase B in phosphate buffered saline (PBS) is injected into the sensor microchannel for 30 min to form a stable monomolecular layer. After the rinsing in PBS buffer, bovine serum albumin (BSA, 0.1 mg/mL) is used for 30 min to deactivate the remaining activated carboxyl sites that did not combine with the RNase B.

Different concentrations of Con A ranging from 0.02 mg/mL to 0.20 mg/mL are monitored by regenerating the biosensor surface. Figure 4b shows the wavelength changes of resonance dip λ_1 with a time resolution of 5 s to dynamically monitor the specific binding between RNase B and Con A. The monitoring process is depicted as follows: First, PBS solution is injected into the flow channel to obtain the baseline. Then, Con A solution is pumped to bind with RNase B on the sensing surface. Next, PBS buffer solution removes the unbound Con A molecules. Finally, the 0.8 mol/L urea solution is used to strip the surface-bound Con A molecules to effectively regenerate the sensing region, and the next concentration can be tested sequentially. As shown in Figure 4b, the baseline of our sensor chip is very stable during the measurement. Abrupt changes of the resonance wavelength after injecting Con A are observed in the sensing curves, which is attributed to the occurrence of specific binding between Con A and RNase B. The association and dissociation rate between Con A and RNase B is also calculated based on sensing curves in Figure 4b. As a contrast, the nonspecific binding between anti-IgG and RNase B does not result in the red shift of resonance wavelength, which illustrates specific binding between Con A and RNase B. To validate reliability and repeatability, each concentration of Con A is measured three times using the same senor chip. The experiment results are summarized in Figure 4c. Determined from the experimental noise and the relationship between the wavelength response and Con A concentration, the detection limit for Con A is estimated to be 4.6 μg/mL (45 nM), which

DOI: 10.1021/acssensors.7b00607
ACS Sens. 2017, 2, 1796−1804

indicates that the PNRA offers a high performance photonic platform for label-free biomolecular detection.

PNRA Integrated on the Optical Fiber for Label-Free Remote Biosensing. As we analyzed above, the subradiant dipolar interactions and lattice plasmon resonance can be excited by the normally incident randomly polarized light. Therefore, the PNRA structure is able to be transferred onto the tip of optical fiber for further integration and miniaturization. Herein we demonstrate an optical fiber biosensor by integrating the PNRA on the fiber tip as a remote biosensing platform. The schematic diagram of the designed optical fiber biosensor is depicted in Figure 5a. The structural parameters of PNRA on the fiber tip are identical to that on the quartz substrate. The designed optical fiber biosensor is fabricated by sequentially depositing 3-nm-thick Ti layer and 100-nm-thick Au film on the fine polishing end face of a 20-cm-long optical fiber (the specification of fiber: core/cladding/coating, 200/220/270 μm; NA $\sim$ 0.22). The PNRA is patterned using FIB over a 150 μm $\times$ 150 μm area. Figure 5b shows SEM and microscope images of the fabricated sample.

To evaluate the sensing performance of optical fiber sensor integrated with PNRA, a homemade flow cell is assembled on the fiber tip. The measured reflectance spectra for the NaCl solutions with different RIs are shown in Figure 5c. The RIs and flow rate of NaCl solutions for the measurement using the optical fiber sensor are identical to that of the quartz substrate device. It can be clearly seen that resonance dip around the wavelength of 755 nm has an obvious red shift and the resonance dip around 850 nm does not vary with the increase of RIs of NaCl solutions. Compared to that of PNRA on the quartz substrate, the line-shape of the resonance dip broadens for the PNRA on the fiber tip because the fiber used in the experiment has a larger NA. The spectral-dip location around the wavelength of 755 nm as a function of RI is depicted in Figure 5d. An RI sensitivity of around 520 nm RIU^{-1} is obtained for the optical fiber sensor, which matches well with that of a quartz substrate device.

Finally, to determine the capability of our designed optical fiber sensor for dynamic monitoring biomolecule interactions, we performed the same experiment to detect in real-time the specific binding of RNase B and Con A protein molecules in solution on the sensing surface. Figure 5e shows the wavelength changes of the resonance dip with a time resolution of 1 s to dynamically monitor the specific binding between RNase B and Con A. Similarly, each concentration of Con A is measured three times using our optical fiber sensor to validate reliability and repeatability. As summarized in Figure 5f, the experiment results imply that the detection limit of optical fiber sensor for Con A is about 6.0 μg/mL (59 nM), very similar to the quartz substrate device. These results confirm that the PNRA offers a high performance photonic platform for the design of miniaturized biosensor for point-of-care and remote biosensing.

DISCUSSION AND CONCLUSION

The designed PNRA sensor has a wide RI detection range. As shown in the Figure S7a, we theoretically investigate the reflectance spectra of the PNRA with the RI range from 1.33 to 1.55. Resonance dip λ_1 always keep narrow line-shape and high peak-to-dip signal ratio within the investigated RI range expect the specific point where there is an intersection between resonance wavelengths λ_1 and λ_2. The PNRA sensor exhibits a good linearity between resonance wavelength λ_1 and RIs in such a large RI range (Figure S7b), which is more superior to that of conventional propagating surface plasmon based sensors.[23,24] Furthermore, although here we design and perform experimental demonstrations on PNRA sensor at visible frequency, its concept and sensing functionality can be easily extended to the infrared range by changing the structural parameters. It is notable that RI sensitivity of the PNRA sensor would increase for the infrared operation frequency because the electromagnetic loss within the metal layer is reduced at longer wavelength. For example, as shown in Figure S5a and b, when the resonance wavelength λ_1 is extended to the wavelength 5000 nm, the RI sensitivity of resonance wavelength λ_1 reaches up to 3800 nm RIU^{-1}. In addition, when the resonance wavelength λ_1 is adjusted from the visible to the infrared region, the line width of the resonance spectrum almost remains unchanged. Therefore, the FOM of the PNRA sensor can also be further increased at longer wavelength.

In summary, we demonstrate a PNRA device which can be used as a high-performance biosensing platform. The coupling of dipolar modes in nanohole and nanodisk arrays gives rise to a robust subradiant lattice plasmon resonance in the PNRA. The narrow spectral line width with high peak-to-dip signal ratio and strong near-field electromagnetic enhancement boost the refractive index sensitivity and FOM associated with the sensing device. In the experimental demonstrations, the PNRA not only realizes high sensitivity refractive index sensing, but also achieves real-time monitoring of biomolecular specific binding interactions at nanomolar concentrations. Compared with other plasmonic sensing devices, the PNRA does not require complicated angular illuminations and has polarization independent optical responses. Due to simple normal illumination and signal acquisition architecture, we transfer the PNRA onto the optical fiber tip and successfully achieve the integrated and remote biosensing. We envision that the PNRA may be a potential candidate for developing a high performance photonic platform for point-of-care, label-free chemical and biomedical sensing.

METHOD

FDTD Simulation. The simulations are performed based on the FDTD algorithm to obtain the reflectance spectra, electric field distribution, and charge distribution of the PNRA at normal incidence. The periodic boundary conditions are applied in both x and y direction and perfectly matched layers are used in the z direction. The grid size along the x, y, and z direction is 2 nm $\times$ 2 nm $\times$ 2 nm, respectively. The dielectric permittivity of bulk gold in the visible and near-infrared region is from Johnson and Christy.[57]

Preparation of Plasmonic Nanoring Resonators Array. First, a 3 nm Ti film and a 100 nm Au film are sputtered sequentially onto a 10 mm $\times$ 10 mm quartz substrate and on the fine polishing end face of a 20-cm-long optical fiber. The deposition rate for Ti and Au is $R_{Ti} \approx 0.016$ nm/s and $R_{Au} \approx 0.05$ nm/s, respectively. Then, subwavelength nanorings are fabricated by FIB milling using a dual-beam (FIB/SEM) system (Ga^+ ions, 24 pA beam current, 30 keV beam energy). The end face of the optical fiber is polished in sequence using a fiber optic polishing machine with 9 μm, 3 μm, 1 μm, 0.03 μm grit emery papers.

Q-Factor Extraction. We use an analytical model to extract the Q-factor of the resonant dip in the PNRA. The calculated and measured spectra are fitted to an analytical model described by $R = |a_1 + ja_2 + b/(\omega - \omega_0 + j\gamma)|^2$, where the parameters a_1, a_2, and b are constant real numbers; the sign j stands for

DOI: 10.1021/acssensors.7b00607
ACS Sens. 2017, 2, 1796−1804

imaginary unit; ω_0 and γ refer to the center resonant frequency and overall damping rate of resonance.[58] The calculated and measured Q-factors are then determined by $Q = (\omega_0/2\gamma)$.

Measurements of Reflectance Spectra. For the structure with PNRA on the quartz substrate, a home-built polydimethylsiloxane (PDMS) flow cell is employed as holder of liquid solution before optical measurement. The flow cell is sandwiched between the sensing substrate and a PMMA plate. Inlet and outlet holes are drilled through the PMMA plate to connect the tubing. All reflectance spectra on the quartz substrate are taken on a UV−vis−NIR microspectrometer (PV20/30 from CRAIC Technologies). For the structure with PNRA on the tip of the optical fiber, a home-built flow cell is used for injection and ejection of sample solutions and the sufficient space for washing sensing surfaces. Light source, spectrometer, and the fiber probe are connected by a binary beam fiber jumper. Light from a halogen lamp (HL-2000-FHSA, Ocean Optics, Inc.) is launched into one splitter end of the fiber jumper. The transmission spectrum is collected at the other splitter end of the fiber jumper through the spectrometer (HR4000, Ocean Optics, Inc.) and is displayed by a computer. The probe is mounted in the combined end of the fiber jumper. In the above optical measurement, a peristaltic pump is used to inject sample solutions with a constant flow rate of 0.2 mL/min.

■ ASSOCIATED CONTENT

Supporting Information

The Supporting Information is available free of charge on the ACS Publications website at DOI: 10.1021/acssensors.7b00607.

Results illustrating a broader line-shape in experiment; electric field distribution at resonant wavelengths for different structures; resonant wavelength and bulk refractive index sensitivity dependent on structure parameters; calculated reflectance spectra for different refractive index solutions; and figure of merit (FOM) of sensing detection (PDF)

■ AUTHOR INFORMATION

Corresponding Authors

*E-mail: yqlu@nju.edu.cn.

*E-mail: xuting@nju.edu.cn.

ORCID

Ting Xu: 0000-0002-0704-1089

Notes

The authors declare no competing financial interest.

■ ACKNOWLEDGMENTS

The work is supported in part by the Ministry of Science and Technology of China under Grant No. 2017YFA0303700, National Natural Science Foundation of China under Grant No. 61705100, 61575092, 61520106013. T. X. acknowledges support from the Thousand Talents Program for Young Professionals and Collaborative Innovations Center of Advanced Microstructures. W. Z. and A. A. acknowledge support under the Cooperative Research Agreement between the University of Maryland and the National Institute of Standards and Technology, Center for Nanoscale Science and Technology, Award#70NANB10H193, through the University of Maryland.

■ REFERENCES

(1) Anker, J. N.; Hall, W. P.; Lyandres, O.; Shah, N. C.; Zhao, J.; Van Duyne, R. P. Biosensing with plasmonic nanosensors. *Nat. Mater.* **2008**, *7*, 442−453.

(2) Mayer, K. M.; Hafner, J. H. Localized surface plasmon resonance sensors. *Chem. Rev.* **2011**, *111*, 3828−3857.

(3) Yanik, A. A.; Huang, M.; Kamohara, O.; Artar, A.; Geisbert, T. W.; Connor, J. H.; Altug, H. An optofluidic nanoplasmonic biosensor for direct detection of live viruses from biological media. *Nano Lett.* **2010**, *10*, 4962−4969.

(4) Liu, N.; Mesch, M.; Weiss, T.; Hentschel, M.; Giessen, H. Infrared perfect absorber and its application as plasmonic sensor. *Nano Lett.* **2010**, *10*, 2342−2348.

(5) Zhang, S.; Bao, K.; Halas, N. J.; Xu, H.; Nordlander, P. Substrate-induced Fano resonances of a plasmonic nanocube: A route to increased-sensitivity localized surface plasmon resonance sensors revealed. *Nano Lett.* **2011**, *11*, 1657−1663.

(6) Verellen, N.; Van Dorpe, P.; Huang, C.; Lodewijks, K.; Vandenbosch, G. A. E.; Lagae, L.; Moshchalkov, V. V. Plasmon line shaping using nanocrosses for high sensitivity localized surface plasmon resonance sensing. *Nano Lett.* **2011**, *11*, 391−397.

(7) Schmidt, M. A.; Lei, D. Y.; Wondraczek, L.; Nazabal, V.; Maier, S. A. Hybrid nanoparticle-microcavity-based plasmonic nanosensors with improved detection resolution and extended remote-sensing ability. *Nat. Commun.* **2012**, *3*, 1108.

(8) Wu, C. H.; Khanikaev, A. B.; Adato, R.; Arju, N.; Yanik, A. A.; Altug, H.; Shvets, G. Fano-resonant asymmetric metamaterials for ultrasensitive spectroscopy and identification of molecular monolayers. *Nat. Mater.* **2011**, *11*, 69−75.

(9) Shen, Y.; Zhou, J. H.; Liu, T. R.; Tao, Y. T.; Jiang, R. B.; Liu, M. X.; Xiao, G. H.; Zhu, J. H.; Zhou, Z. K.; Wang, X. H.; Jin, C. J.; Wang, J. F. Plasmonic gold mushroom arrays with refractive index sensing figures of merit approaching the theoretical limit. *Nat. Commun.* **2013**, *4*, 2381.

(10) Li, N.; Tittl, A.; Yue, S.; Giessen, H.; Song, C.; Ding, B.; Liu, N. DNA-assembled bimetallic plasmonic nanosensors. *Light: Sci. Appl.* **2014**, *3*, e226.

(11) Feng, J.; Pacifici, D. A spectroscopic refractometer based on plasmonic interferometry. *J. Appl. Phys.* **2016**, *119*, 083104.

(12) Li, D.; Feng, J.; Pacifici, D. Nanoscale optical interferometry with incoherent light. *Sci. Rep.* **2016**, *6*, 20836.

(13) Hui, Y.; Gomez-Diaz, J. S.; Qian, Z.; Andrea, A.; Rinaldi, M. Plasmonic piezoelectric nanomechanical resonator for spectrally selective infrared sensing. *Nat. Commun.* **2016**, *7*, 11249.

(14) Zhao, Y.; Askarpour, A. N.; Sun, L.; Shi, J.; Li, X.; Andrea, A. Chirality detection of enantiomers using twisted optical metamaterials. *Nat. Commun.* **2017**, *8*, 14180.

(15) Yuan, J.; Duan, R.; Yang, H.; Luo, X.; Xi, M. Detection of serum human epididymis secretory protein 4 in patients with ovarian cancer using a label-free biosensor based on localized surface plasmon resonance. *Int. J. Nanomed.* **2012**, *7*, 2921−2928.

(16) Zhang, K.; Zhang, L.; Yap, F. L.; Song, P.; Qiu, C. W.; Loh, K. P. Large-area graphene nanodot array for plasmon-enhanced infrared spectroscopy. *Small* **2016**, *12*, 1302−1308.

(17) Peng, L.; Zhang, L.; Yuan, J.; Chen, C.; Bao, Q.; Qiu, C. W.; Peng, Z.; Zhang, K. Gold nanoparticle mediated graphene plasmon for broadband enhanced infrared spectroscopy. *Nanotechnology* **2017**, *28*, 264001.

(18) Yuan, Y. J.; Jia, R. Study on pivot-point vibration of molecular bond-rupture events by quartz crystal microbalance for biomedical diagnostics. *Int. J. Nanomed.* **2012**, *7*, 381−391.

(19) Feng, J.; Li, D.; Pacifici, D. Circular slit-groove plasmonic interferometers: a generalized approach to high-throughput biochemical sensing. *Opt. Mater. Express* **2015**, *5*, 2742−2753.

(20) Siu, V. S.; Feng, J.; Flanigan, P. W.; Palmore, G. T. R.; Pacifici, D. A "plasmonic cuvette": dye chemistry coupled to plasmonic interferometry for glucose sensing. *Nanophotonics* **2014**, *3*, 125−140.

(21) Feng, J.; Siu, V. S.; Roelke, A.; Mehta, V.; Rhieu, S. Y.; Palmore, G. T. R.; Pacifici, D. Nanoscale plasmonic interferometers for

DOI: 10.1021/acssensors.7b00607
ACS Sens. 2017, 2, 1796−1804

multispectral, high-throughput biochemical sensing. *Nano Lett.* **2012**, *12*, 602−609.
(22) Rothenhäusler, B.; Knoll, W. Surface-plasmon microscopy. *Nature* **1988**, *332*, 615−617.
(23) Homola, J.; Yee, S. S.; Gauglitz, G. Surface plasmon resonance sensors: Review. *Sens. Actuators, B* **1999**, *54*, 3−15.
(24) Homola, J. Surface plasmon resonance sensors for detection of chemical and biological species. *Chem. Rev.* **2008**, *108*, 462−493.
(25) Luppa, P. B.; Müller, C.; Schlichtiger, A.; Schlebusch, H. Point-of-care testing (POCT): Current techniques and future perspectives. *TrAC, Trends Anal. Chem.* **2011**, *30*, 887−898.
(26) Jensen, T. R.; Malinsky, M. D.; Haynes, C. L.; Van Duyne, R. P. Nanosphere lithography: tunable localized surface plasmon resonance spectra of silver nanoparticles. *J. Phys. Chem. B* **2000**, *104*, 10549−10556.
(27) Malinsky, M. D.; Kelly, K. L.; Schatz, G. C.; Van Duyne, R. P. Chain length dependence and sensing capabilities of the localized surface plasmon resonance of silver nanoparticles chemically modified with alkanethiol self-assembled monolayers. *J. Am. Chem. Soc.* **2001**, *123*, 1471−1482.
(28) Hao, F.; Sonnefraud, Y.; Van Dorpe, P.; Maier, S. A.; Halas, N. J.; Nordlander, P. Symmetry breaking in plasmonic nanocavities: Subradiant LSPR sensing and a tunable Fano resonance. *Nano Lett.* **2008**, *8*, 3983−3988.
(29) Sonnefraud, Y.; Verellen, N.; Sobhani, H.; Vandenbosch, G. A. E.; Moshchalkov, V. V.; Van Dorpe, P.; Nordlander, P.; Maier, S. A. Experimental realization of subradiant, superradiant, and Fano resonances in Ring/Disk plasmonic nanocavities. *ACS Nano* **2010**, *4*, 1664−1670.
(30) Cetin, A. E.; Altug, H. Fano resonant ring/disk plasmonic nanocavities on conducting substrates for advanced biosensing. *ACS Nano* **2012**, *6*, 9989−9995.
(31) Fan, J. A.; Wu, C.; Bao, K.; Bao, J.; Bardhan, R.; Halas, N. J.; Manoharan, V. N.; Nordlander, P.; Shvets, G.; Capasso, F. Self-assembled plasmonic nanoparticle clusters. *Science* **2010**, *328*, 1135−1138.
(32) Lassiter, J. B.; Sobhani, H.; Fan, J. A.; Kundu, J.; Capasso, F.; Nordlander, P.; Halas, N. J. Fano resonances in plasmonic nanoclusters: geometrical and chemical tunability. *Nano Lett.* **2010**, *10*, 3184−3189.
(33) Alonso-Gonzalez, P.; Schnell, M.; Sarriugarte, P.; Sobhani, H.; Wu, C.; Arju, N.; Khanikaev, A.; Golmar, F.; Albella, P.; Arzubiaga, L.; Casanova, F.; Hueso, L. E.; Nordlander, P.; Shvets, G.; Hillenbrand, R. Real-space mapping of Fano interference in plasmonic metamolecules. *Nano Lett.* **2011**, *11*, 3922−3926.
(34) König, M.; Rahmani, M.; Zhang, L.; Lei, D. Y.; Roschuk, T. R.; Giannini, V.; Qiu, C. W.; Hong, M. H.; Schlücker, S.; Maier, S. A. Unveiling the correlation between nanometer-thick molecular monolayer sensitivity and near-field enhancement and localization in coupled plasmonic oligomers. *ACS Nano* **2014**, *8*, 9188−9198.
(35) Zou, S. L.; Janel, N.; Schatz, G. C. Silver nanoparticle array structures that produce remarkably narrow plasmon lineshapes. *J. Chem. Phys.* **2004**, *120*, 10871−10875.
(36) Auguie, B.; Barnes, W. L. Collective resonances in gold nanoparticle arrays. *Phys. Rev. Lett.* **2008**, *101*, 143902.
(37) Vecchi, G.; Giannini, V.; Rivas, J. G. Shaping the fluorescent emission by lattice resonances in plasmonic crystals of nanoantennas. *Phys. Rev. Lett.* **2009**, *102*, 146807.
(38) Zhou, W.; Odom, T. W. Tuanable subradiant lattice plasmons by out-of-plane dipolar interactions. *Nat. Nanotechnol.* **2011**, *6*, 423−427.
(39) Kabashin, A. V.; Evans, P.; Pastkovsky, S.; Hendren, W.; Wurtz, G. A.; Atkinson, R.; Pollard, R.; Podolskiy, V. A.; Zayats, A. V. Plasmonic nanorod metamaterials for biosensing. *Nat. Mater.* **2009**, *8*, 867−871.
(40) Sreekanth, K. V.; Alapan, Y.; ElKabbash, M.; Ilker, E.; Hinczewski, M.; Gurkan, U. A.; De Luca, A.; Strangi, G. Extreme sensitivity biosensing platform based on hyperbolic metamaterials. *Nat. Mater.* **2016**, *15*, 621−627.
(41) Luk'yanchuk, B.; Zheludev, N. I.; Maier, S. A.; Halas, N. J.; Nordlander, P.; Giessen, H.; Chong, C. T. The Fano resonance in plasmonic nanostructures and metamaterials. *Nat. Mater.* **2010**, *9*, 707−715.
(42) Miroshnichenko, A. E.; Flach, S.; Kivshar, Y. S. Fano resonances in nanoscale structures. *Rev. Mod. Phys.* **2010**, *82*, 2257−2298.
(43) Hao, F.; Nordlander, P.; Sonnefraud, Y.; Van Dorpe, P.; Maier, S. A. Tunability of subradiant dipolar and Fano-type plasmon resonances in metallic ring/disk cavities: Implications for nanoscale optical sensing. *ACS Nano* **2009**, *3*, 643−652.
(44) Consales, M.; Ricciardi, A.; Crescitelli, A.; Esposito, E.; Cutolo, A.; Cusano, A. Lab-on-fiber technology: Toward multifunctional optical nanoprobes. *ACS Nano* **2012**, *6*, 3163−3170.
(45) Ricciardi, A.; Crescitelli, A.; Vaiano, P.; Quero, G.; Consales, M.; Pisco, M.; Esposito, E.; Cusano, A. Lab-on-fiber technology: a new vision for chemical and biological sensing. *Analyst* **2015**, *140*, 8068−8079.
(46) Kostovski, G.; Stoddart, P. R.; Mitchell, A. The optical fiber tip: An inherently light-coupled microscopic platform for micro- and nanotechnologies. *Adv. Mater.* **2014**, *26*, 3798−3820.
(47) Cusano, A.; Consales, M.; Crescitelli, A.; Ricciardi, A. *Lab-On-Fiber Technology*; Springer, 2015.
(48) Morrill, D.; Li, D.; Pacifici, D. Measuring subwavelength spatial coherence with plasmonic interferometry. *Nat. Photonics* **2016**, *10*, 681−687.
(49) Li, D.; Feng, J.; Pacifici, D. Higher-order surface plasmon contributions to passive and active plasmonic interferometry. *Opt. Express* **2016**, *24*, 27309−27318.
(50) Prodan, E.; Radloff, C.; Halas, N. J.; Nordlander, P. A hybridization model for the plasmon response of complex nanostructures. *Science* **2003**, *302* (5644), 419−422.
(51) Clausen, J. S.; Hojlund-Nielsen, E.; Christiansen, A. B.; Yazdi, S.; Grajower, M.; Taha, H.; Levy, U.; Kristensen, A.; Mortensen, N. A. Plasmonic metasurfaces for coloration of plastic consumer products. *Nano Lett.* **2014**, *14*, 4499−4504.
(52) Verellen, N.; Sonnefraud, Y.; Sobhani, H.; Hao, F.; Moshchalkov, V. V.; Dorpe, P. V.; Nordlander, P.; Maier, S. A. Fano resonances in individual coherent plasmonic nanocavities. *Nano Lett.* **2009**, *9*, 1663−1667.
(53) Zhang, L.; Dong, Z.; Wang, Y. M.; Liu, Y. J.; Zhang, S.; Yang, J. K. W.; Qiu, C. W. Dynamically configurable hybridization of plasmon modes in nanoring dimer arrays. *Nanoscale* **2015**, *7*, 12018−12022.
(54) Liu, Y.; Liu, Q.; Chen, S.; Cheng, F.; Wang, H.; Peng, W. Surface plasmon resonance biosensor based on smart phone platforms. *Sci. Rep.* **2015**, *5*, 12864.
(55) Cheng, F.; Shang, J.; Ratner, D. M. A versatile method for functionalizing surfaces with bioactive glycans. *Bioconjugate Chem.* **2011**, *22*, 50−57.
(56) Liu, Y.; Chen, S.; Liu, Q.; Masson, J.-F.; Peng, W. Compact multi-channel surface plasmon resonance sensor for real-time multi-analyte biosensing. *Opt. Express* **2015**, *23*, 20540−20548.
(57) Johnson, P. B.; Christy, R. W. Optical constants of noble metals. *Phys. Rev. B* **1972**, *6*, 4370−4379.
(58) Yang, Y.; Kravchenko, I. I.; Briggs, D. P.; Valentine, J. All-dielectric metasurface analogue of electromagnetically induced transparency. *Nat. Commun.* **2014**, *5*, 5753.

DOI: 10.1021/acssensors.7b00607
ACS Sens. 2017, 2, 1796−1804